

## 5 Rear Wing Study

In this section the results of the three-dimensional simulation are reported. Running different cases, a brief mesh analysis was performed in order to assure that the insight acquired from the two-dimensional simulation could be transferred to the three-dimensional analysis. Finally, the results of the flow simulation around the rear wing are visualized, commented and discussed.

### 5.1 Test case (description)

The geometry employed in the three-dimensional simulations was the rear wing of the PUC-Rio Formula car. It is mounted on an aluminum support directly bolted to the gearbox as shown below in Fig 5.1. It is composed by a rectangular inverted wing with a total span of  $1.125[m]$ , with end plates at the tips.



Figure 5.1: Formula car

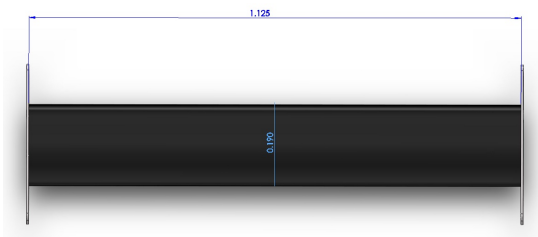
The cross section of the wing (airfoil) does not correspond to any particular aerodynamic profile, so its geometry was acquired using a three-dimensional scanner shown at the top of Fig 5.2. After acquiring that geometry, it was processed in SolidWorks to model and generate a complete 3D object.

Figure 5.2 part c) shows the single-element airfoil comprising the rear wing cross-section. It is a high cambered airfoil with a chord length of  $0.19[m]$ . The curvature of both the leading edge and the trailing edge were kept as were

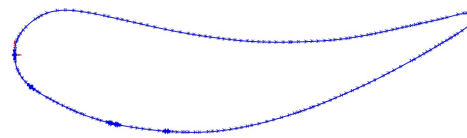
scanned from the real element and its current position was considered as being the  $0^\circ$  of incidence.



a) Scanning process



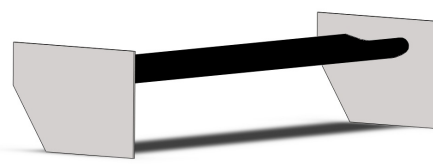
b) Spanwise view



c) Airfoil geometry



d) 3D model



e) Cleaned geometry

Figure 5.2: Wing geometry

The geometry was then cleaned up in preparation for the grid generation to avoid particular features such as chamfered corners, tiny faces or short edges, which could produce highly skewed cells or obstruct the normal generation of the grid. The elimination of these features was considered not to influence significantly the simulation results, but to improve the grid quality. The resulting rear wing after the cleaned up process is shown in Fig 5.2 part e).

Using the knowledge gained during the two-dimensional grid generation and doing some simplifications to decrease the total number of nodes, the computational domain around the wing was generated keeping the same basic criteria that gave the best results in the former chapter; such as local refinement and hexahedral layers around the wing surface.

Since the flow is expected to be symmetric around the mid plane of the wing, only one half of the domain was simulated. This simplification is normally used to reduce the total number of cells, so that the computational requirements needed to solve the simulation are also reduced.

The computational domain, shown in Fig 5.3, consists of six external boundaries (inlet, outlet, back, front, bottom, top) and an internal one (rear-Wing). A refinement box is placed inside the domain where the majority of cells are concentrated. The origin of the coordinate system  $(0, 0, 0)$  is located at the leading edge, at the intersection of the wing and the symmetry plane. The wing is placed at 1 [m] above the bottom plane and the angle of attack is changed rotating the wing geometry before the grid generation. To illustrate the resulting grid, figure 5.3 shows an example of the grid layout.

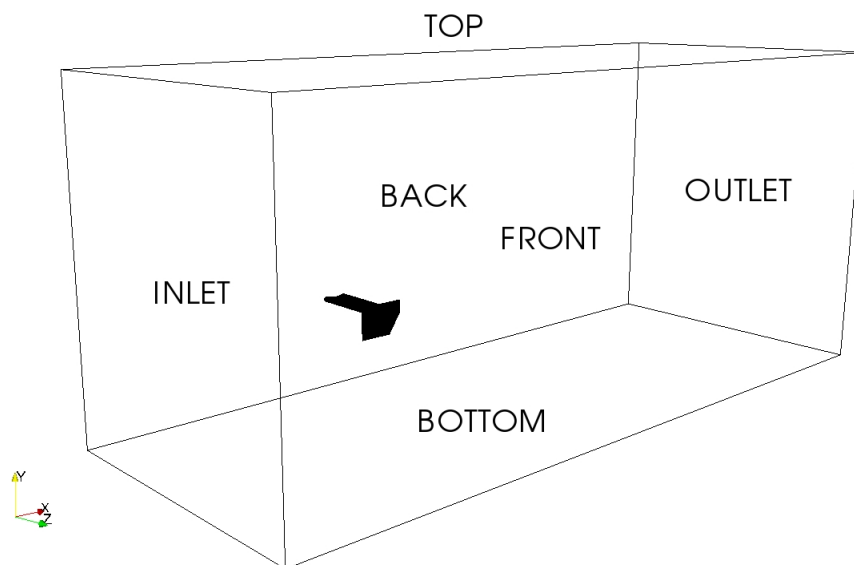


Figure 5.3: Computational domain

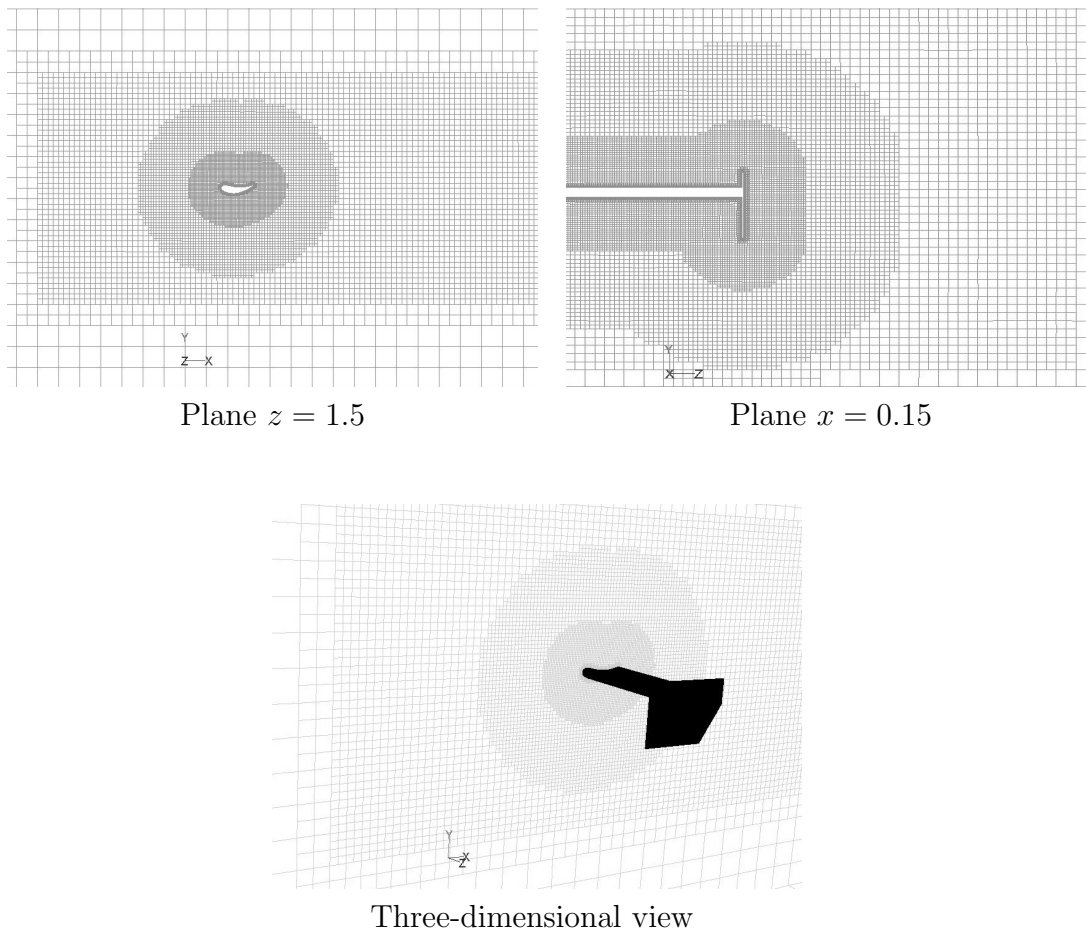


Figure 5.4: Example of the cells distribution on Grid M10

Six different grids were created setting up six different sets of refinement parameters. As in the two-dimensional grids, the main geometrical parameters to be changed were the length and the height of the cells in the near-wall layers. The third component ( $z$  direction) refinement is performed based on the same general parameters used for the other directions. The resulting features of the six grids are shown in table 5.1.

Two of these six grids do not have near-wall layers [M0, M1]. The last four grids [M10, M15, M20, M21] are build-up with near-wall layers. Generating near-wall layers increases radically the total numbers of cells, as the table shows below. For example, grids M10, M15, and M20 have almost twice more cells than M0 for the same total refinement ratio.

Grid	N. of Cells	non-Orthogonality	Max. Skewness
M0	1065328	26.97	0.85
M1	2045619	26.27	1.08
M10	1862173	64.55	1.29
M15	1643133	57.92	2.23
M20	2014783	54.80	2.49
M21	7928824	64.89	1.88

Table 5.1: Grid features

At this point it is important to bring attention to the weakness of the grids generated with **snappyHexMesh** for three-dimensional geometries. Firstly, the addition of near-wall layers does not work properly at intersections. Layers are reduced or simply are not generated at all close to steep changes between two surfaces. This shortcoming produced a local increase of non-hexahedral elements and varied the  $y^+$  values at that locations. Secondly, the snapping function produced some unwanted geometry features at the surface when the grade of refinement was not enough to contour the geometry curvature.

### 5.1.1

#### Boundary conditions

Average conditions of velocity and turbulence were considered to set the boundary conditions. A constant value of 120 [ $km/h$ ] (33.3 [ $m/s$ ]) in the  $x$  direction was set as inlet velocity. This value corresponds to an average velocity selected according to the expected performance of the formula car. As a result, the Reynolds number based on this free stream velocity and the chord length is  $4.2 \times 10^5$ .

The free stream turbulence intensity was tested to evaluate its influence in the simulation results. Two typical values for wind tunnel experiments were employed (0.3% and 1%), which did not affected significantly the computed velocity field. The other boundary conditions were set as follows:

- Rear wing and end plate

Set as walls, non-slip condition.

- Bottom surface (the ground)

Set as symmetry. The basic idea here is that the symmetry line that is supposed to divide two models is also a stream line. Therefore, the moving-ground simulation is automatically obtained. [28].

- Back surface

Set as symmetry. Here lies the symmetry plane that divides the rear wing in the middle.

- Front and Top surfaces

Set as wall, non-slip condition.

- Outlet surface

Set as outflow.

## 5.2

### Results

The analysis and discussion of the results is divided in two parts. First, some control points to evaluate the grid features are presented, followed by the results of the aerodynamic coefficients in order to assess the performance of the six grids mentioned above. Second, the characteristics of the flow, for two angles of attack, is analyzed based on the pressure distribution and flow visualization. The aim of these tests is to know how the results vary in regard to the degree of refinement of the grid and the type of turbulence model.

#### 5.2.1

##### Iterative Convergence

The solution convergence was monitored using the residuals of the governing equations. Figure 5.5 shows four examples of the residuals evolution for  $0^\circ$  and  $0^\circ$  of incidence. In these examples as in the majority of the simulations, the residuals were higher than those obtained in the two-dimensional simulations.

The oscillations in the residuals was a matter of concern. In spite of the efforts to reduce them, it was not possible to obtain a simulation without oscillations in the residuals. First order and second order discretization schemes were tested to clarify their origin, but no clear explanation was found because in both cases similar oscillation patterns appeared. However, since the residuals oscillates around a constant value close to the convergence criterion, the results were considered as converged.

#### 5.2.2

##### Near-wall Behavior

As it was already mentioned,  $y^+$  values of the first nodes around the wing are a useful criterion in the assessment of the grid. Contours of  $y^+$  for  $0^\circ$  and  $15^\circ$  of flow incidence on the wing are presented in Fig 5.6. They show high values where the mesh near-wall layers were incorrectly generated or where they were not generated at all. That is, the first nodes in these regions are higher than

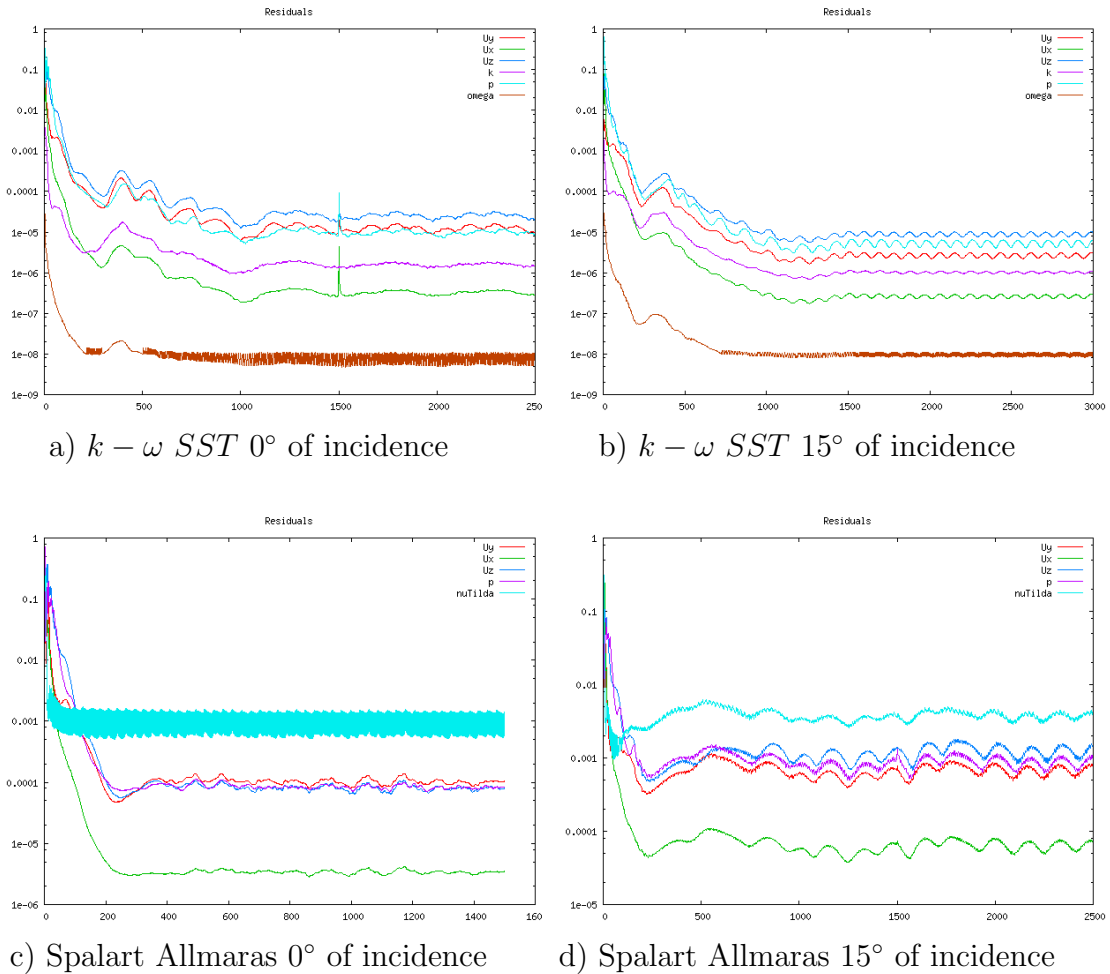
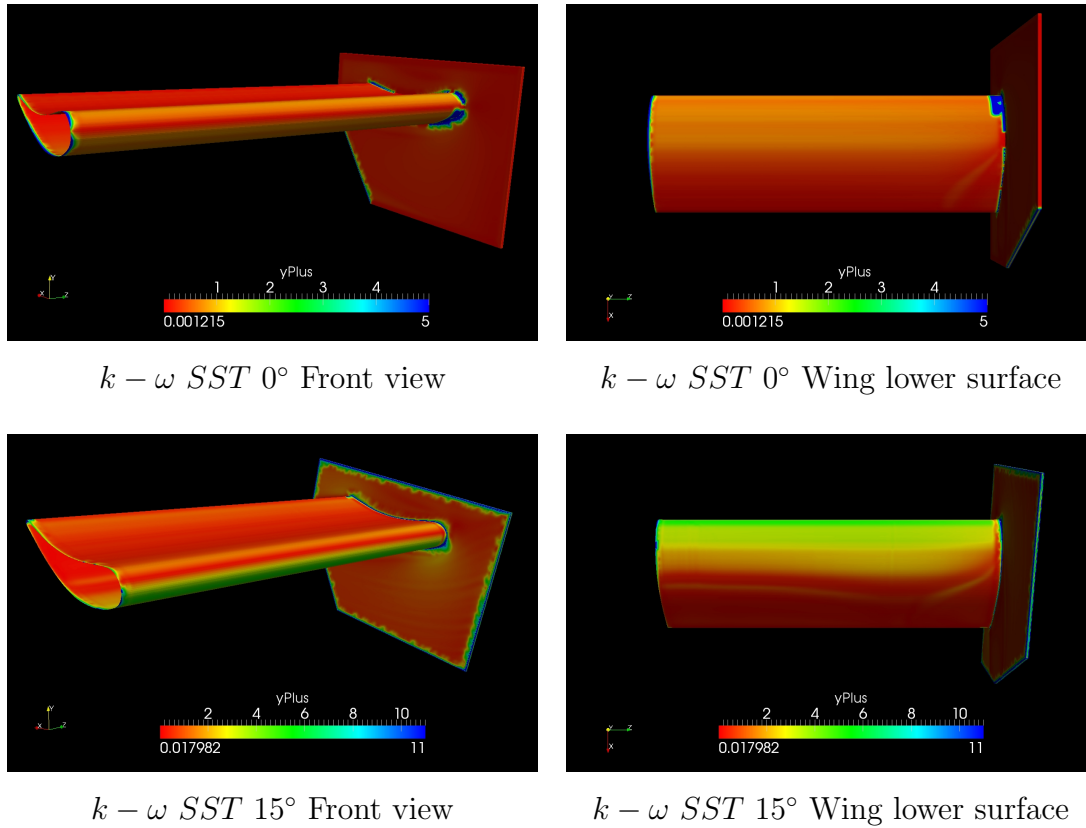


Figure 5.5: Residuals grid [M10]

those located where the layers were correctly generated. The junction between the wing tip and end plate along with the opposite tip, where the symmetry is placed, are examples of that places in the grid.

Observing the data in Fig 5.6, it is also possible to note how the  $y^+$  values change along the wing and the end plate in the streamwise direction. They are pretty high at the stagnations points, since in that locations the boundary layer is inexistent or rather small. Afterwards, they decrease along the chord at the upper surface, since the thickness of the boundary layer increases and shear stress diminishes. On the suction surface, the values of  $y^+$  increases along the chordwise as the velocity increases near to the leading edge, showing that the boundary layer thickness decreases due to the higher velocity under the wing. After reaching its top value at the maximum thickness, the velocity starts to decrease, which results in a progressive increase of the boundary layer and therefore a decrease in the  $y^+$  values.

Figure 5.6: Distribution of  $y^+$  values on the wing surface grid M10

### 5.2.3 Aerodynamic Coefficients

Figure 5.7 shows the variation with the angle of attack of the lift coefficient  $C_L$  for the  $k - \omega SST$  model, obtained with different mesh distributions. It can be seen that the results follow a growing trend, which is coherent with the wing theory. Comparing the results of each grid, it is clear that the grids without near-wall layers, [M0, M1], predicts larger values of  $C_L$  compared to those using them. Whereas, [M15] having the largest value of  $y^+$  ( $y^+ > 30$ ), predicts lower values of  $C_L$  compared with the finer grids. Grid [M20] presents larger values of lift, following the pattern in the results found for grids with lower aspect-ratio cells near the wall in the former chapter. Comparing the finer grids [M10, M21], it can be noted that they present similar results, which suggests grid convergence.

From these results it is possible to conclude that the use of near-wall layers affects largely the predicted values of lift coefficients. In fact, for the same level of refinement, e.g., grids [M1] and [M21], the results obtained without near-wall layers in [M1] are not consistent considering that the results of the finer grid [M21] are the best, which means that grid convergence is not

reached. This was also the case for the two-dimensional simulations, as shown in chapter 4. According to John Wendt [37], the discrepancy in the previously mentioned results can be explained, since the alignment of the grid with the flow provided by the near wall layers leads to less numerical diffusion in the streamlines direction. In fact, if these aligned cell layers have a high aspect ratio, numerical diffusion was found to be further reduced.

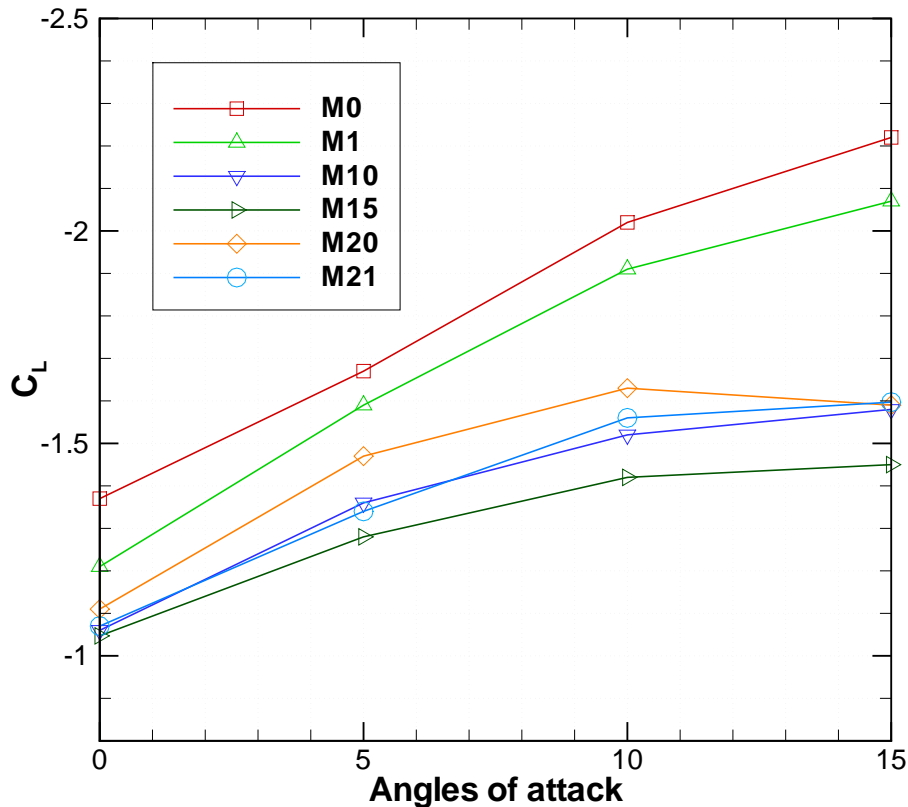


Figure 5.7: Mesh influence in  $C_L$  results using  $k - \omega SST$  model

It can be noticed from this figure that the results are quite sensitive to the first layer height. Comparing [M10, M20, M21] with [M15] it is obvious that the location of the first nodes affected the manner that the turbulence model solved the flow near the wall.

The results of the lift coefficient predicted by the Spalart Allmaras model are presented in Fig 5.8. In this case, the results follow the same growing trend as those in the previous figure. Lift coefficients are larger in the [M0] and [M1] grids and accordingly to what was found in the two-dimensional validation the coarsest grid, [M15], also predicted larger values of lift compared with the

finer grids. The difference among the finer three grids [M10, M20, M21] is smaller having almost the same values for all the angles of attack. Compared to the previous model, the Spalart Allmaras predicted larger values of  $C_L$  in the coarser grids [M0, M1]. Comparing figure 5.7 and 5.8 one can notice that the  $k - \omega SST$  model is more sensitive to the near-wall grid refinement than the Spalart Allmaras model.

Furthermore, the lift values predicted by this model in the finer grids are lower than those predicted by the  $k - \omega SST$ . This can be seen in Fig 5.9 where all the resulting values of  $C_L$  are depicted. The difference at each angle of attack between both turbulence models is considerable and grows as the angle of attack grows. This is due the fact that each turbulence model computes turbulence in a different manner, which results in significant disagreement in the prediction of separation.

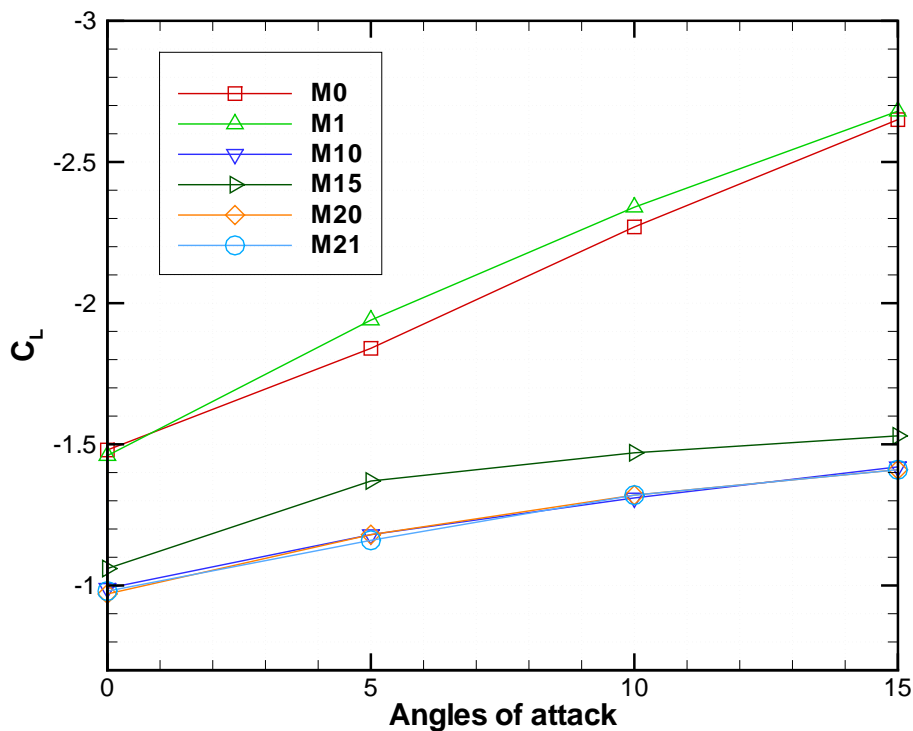


Figure 5.8: Mesh influence in  $C_L$  results using Spalart Allmaras model

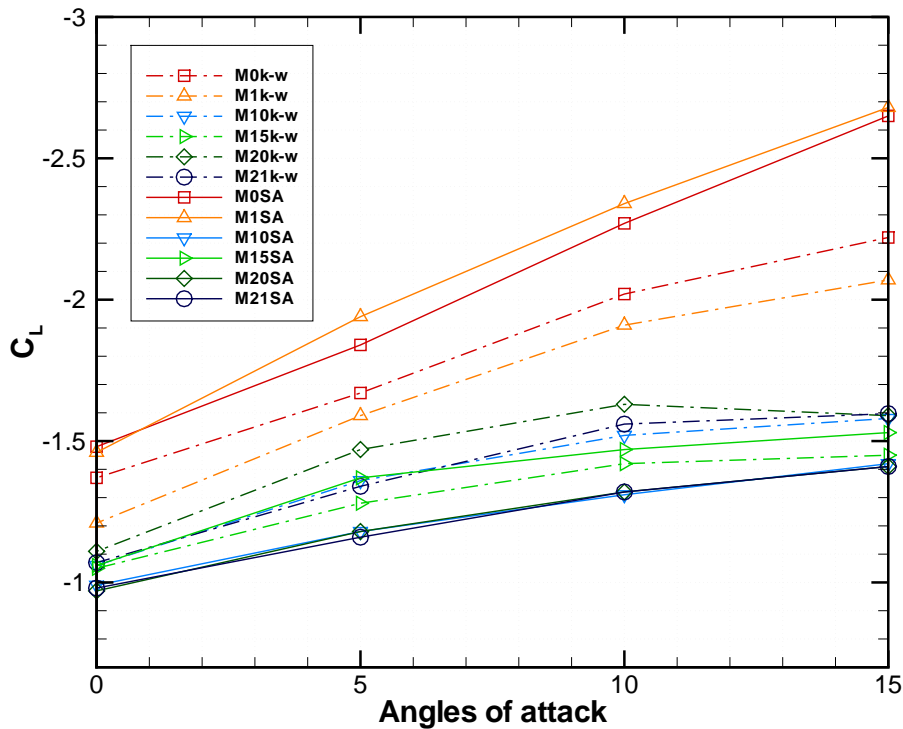


Figure 5.9: Mesh influence in the lift coefficient for the Spalart Allmaras and  $k - \omega$  SST models

Figures 5.10 and 5.11 present the drag coefficient variation with the angle of attack for all meshes and for each turbulence model, respectively. Good agreement was obtained for the finer grids. The curves show a growing trend as the angles of attack increases, as expected, this trend confirms that the drag coefficient increases as the angle of attack increases. Similar to the lift coefficient, the discrepancy among the results grows with the angle of attack due to different level in the prediction of boundary-layer separation. Furthermore, it is interesting to note that the grid refinement affects in a greater manner the prediction of drag than the prediction of lift. This is due to the fact that not only the near-wall refinement is important to calculate the drag, but also the near velocity field affecting the pressure around the wing. In other words, since the drag is the resultant of three different effects (skin friction, pressure drag and induced drag), its accurate prediction depends on the grid being able to capture all the physics of the flow, namely, friction at walls, separation, and tip vortex structures effects.

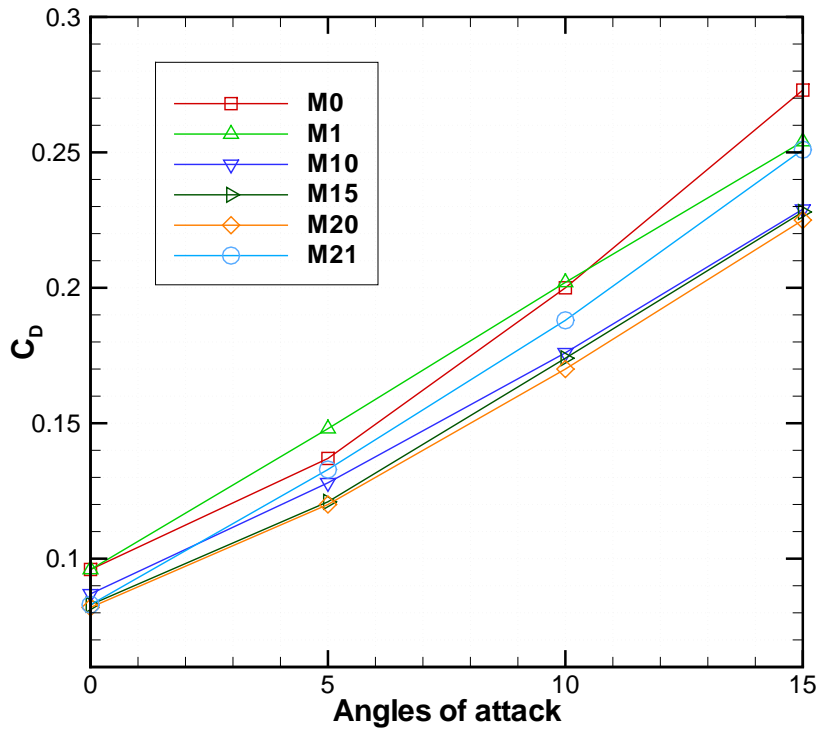


Figure 5.10:  $C_D$  results using  $k - \omega SST$  model

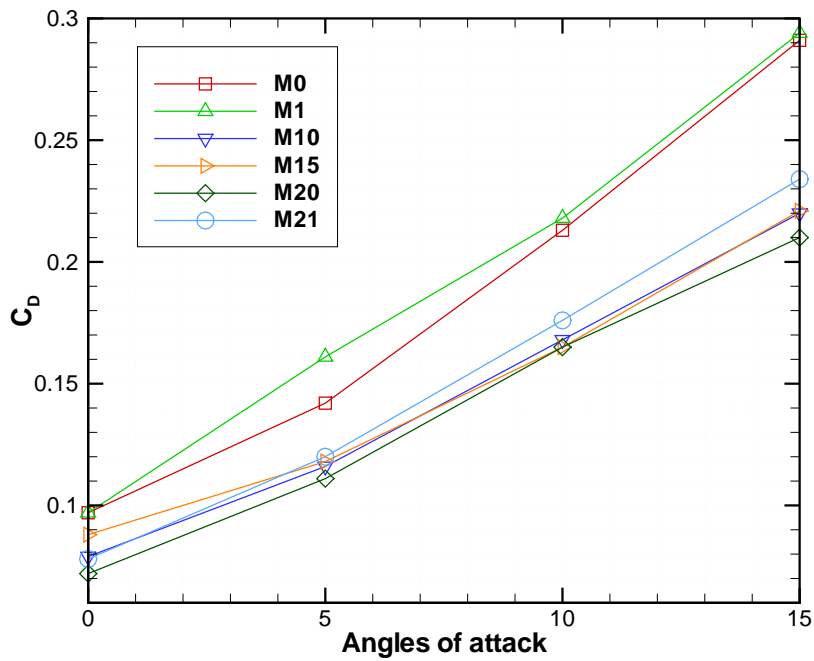


Figure 5.11:  $C_D$  results using Spalart Allmaras

#### 5.2.4 Pressure Distribution

The flow around the rear wing presented interesting structures, which were observed visualizing the flow through contours, streamlines and iso-surfaces.

Figure 5.12 shows the three-dimensional pressure contours over the surface of the rear wing for  $0^\circ$  of incidence. In this figure, both turbulence models predict similar pressure distributions, with a slight difference in the minimum pressure value. The region where the contour is blue indicates the stagnation zone along the leading edge, which has the highest value of pressure. The fluid is then split into two streams, one heading the upper surface and the other to the bottom surface of the wing. In the upper surface, the fluid suffers a small gain of speed due to the leading edge curvature but then it is decelerated towards the mid and aft section of the airfoil. In the lower surface, the rapid acceleration of the fluid over the forward portion of the wing is characterized by a strong decrease in the pressure, localized in the most cambered part of the lower surface (yellow and red zones). This low pressure region is followed by a pressure raise (green zone) due to the progressive deceleration of the fluid towards the trailing edge. The aforementioned pressure distribution is also impressed in the internal face of the end plate, since it receives the same influence of the flow exerted near the wing tip.

In addition, it is important to note that the pressure field is affected by the proximity of the wing tip, specially on the suction surface. It seems that such alteration is due to the influence of the tip vortex originated by the strong pressure difference between the upper and lower surface. As a result, the total downforce is reduced and the drag is increased. This pattern in the surface pressure is predicted for both turbulence models, although the influence zone predicted by the  $k-\omega$  SST model is larger than that predicted by the Spalart Allmaras model.

Figure 5.13 shows the pressure contour for  $15^\circ$  of incidence. Here, a much lower pressure on the wing bottom is produced due the considerable velocity induced by the larger angle of attack. Small changes were produced in the pressure distribution on the upper surface, although comparing it with the former figure, the velocity at the trailing edge is much smaller. An additional effect of the larger angle of attack is the boundary layer separation (showed in dark green) located on the aft portion of the lower surface. It is the result of the abrupt rise in the pressure due to the strong fluid deceleration in the middle of the suction surface of the wing. This zone is characterized by flow recirculation and lost of aerodynamic pressure (negative pressure). Another important feature that must be pointed out is again the influence of the tip

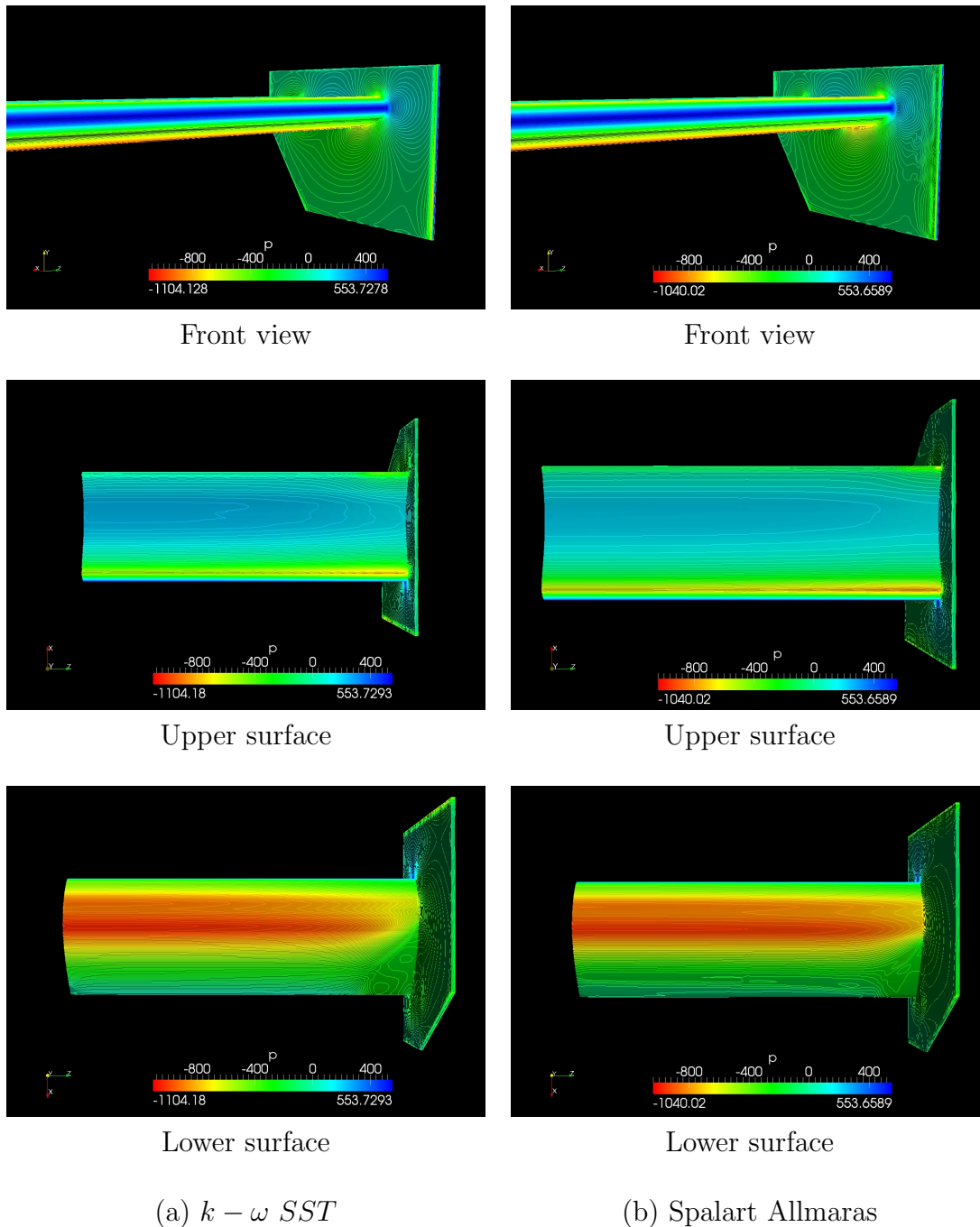


Figure 5.12: Computed pressure contours on the wing surface for  $0^\circ$  of incidence vortex. In this case, unlike the former case, it helps to prevent the boundary layer separation in the vicinity of the wing tip. It seems that part of the vortex kinetic energy is transferred to the oncoming flow allowing it to keep attached to the surface for a little more distance. In this regard, the  $k - \omega SST$  model predicted a bigger influence, meaning less separation than the Spalart Allmaras model, which translates in more lift and less drag.

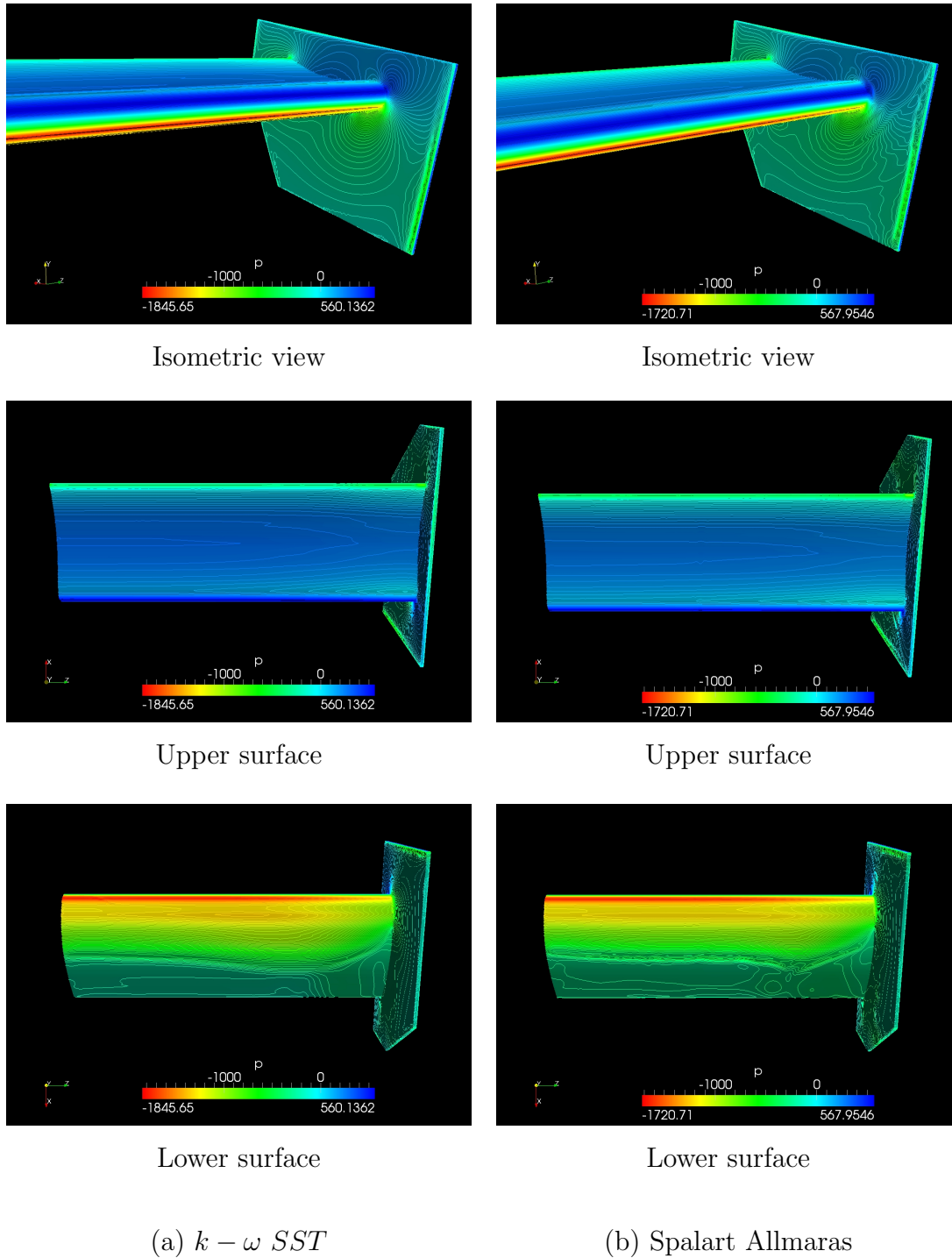


Figure 5.13: Computed pressure contours on the wing surface for  $15^\circ$  of incidence

In order to clarify how the pressure varies along the wing in the stream-wise direction, five planes along the wing spanwise direction were selected to plot the pressure coefficient versus the cord length. Figure 5.14 shows these plots for two angles of attack and both turbulence models.

For  $0^\circ$  of incidence, the pressure coefficient in the upper surface starts

at the maximum value corresponding to the low speed at the foremost point. Then it drops and rises steeply in the excessively rounded vicinity of the leading edge. After passing this region it continues to grow until it reaches the trailing edge neighborhood, then it drops again due to the extremely rounded form of the trailing edge. In similar way, the pressure in the lower surface starts dropping from the maximum value in the leading edge, but in this case it continues dropping almost to the middle of wing where the pressure starts growing until the trailing edge. From 80% of the wing span onwards, the effects of the wing tip vortex can be noticed in the decrease of the pressure distribution. The boundary layer separation can be easily distinguished, as it can be associated to constant pressure regions in the pressure distribution. Comparing the turbulence models, it can be observed that the  $k-\omega SST$  model predicts a wider attached region on the suction surface even in the middle of the wing ( $z/s = 0$ ). This behavior affects directly the overall lift value, but does not justify the discrepancy between the results predicted by both models, since the minimum pressure predicted by the Spalart Allmaras model is indeed higher compared to the pressure predicted by the  $k-\omega SST$  model.

For  $15^\circ$  of incidence, the trend in the  $C_p$  distribution is totally different. The steep pressure drop in the leading edge is no longer seen, because the angle of incidence shifted the stagnation point to a higher position, avoiding the excessive acceleration in this part of the wing. The suction surface also presents a different distribution; here the maximum acceleration is reached very close to the leading edge, after which a greater adverse pressure region is observed. This increased adverse pressure region generates a premature separation of the boundary layer, which can be seen in Fig 5.14 as a constant value region in the pressure distribution along the wing span. Moreover, it can be observed a positive influence on the pressure distribution due to the tip vortex, since the pressure distribution in the planes near the tip ( $z/s = 0.8$  and  $z/s = 0.9$ ) presents values of  $C_p$  even larger than those in the middle of the wing ( $z/s = 0$ ). This influence remains positive only to the 80% of the wing span, where the tip vortex influence becomes negative promoting early boundary layer separation. Also, it is interesting to note the peaks in the pressure distribution just before the boundary separation. This feature is more pronounced in the Spalart Allmaras model, but it is present in both turbulence models. It seems that this pressure peak corresponds to a boundary layer reattachment after a recirculation tube which extends along the wing span.

Based on these results, one can observe that, while wing tip vortex promotes boundary separation in the vicinity of the wing and end plate

junction for both angle of attack, it helps delaying separation at a region located around 80% of the wingspan for higher attack. The net effect is decrease in lift and increase in drag for low angle of attack, and increase in lift and decrease in drag for high angle of attack.

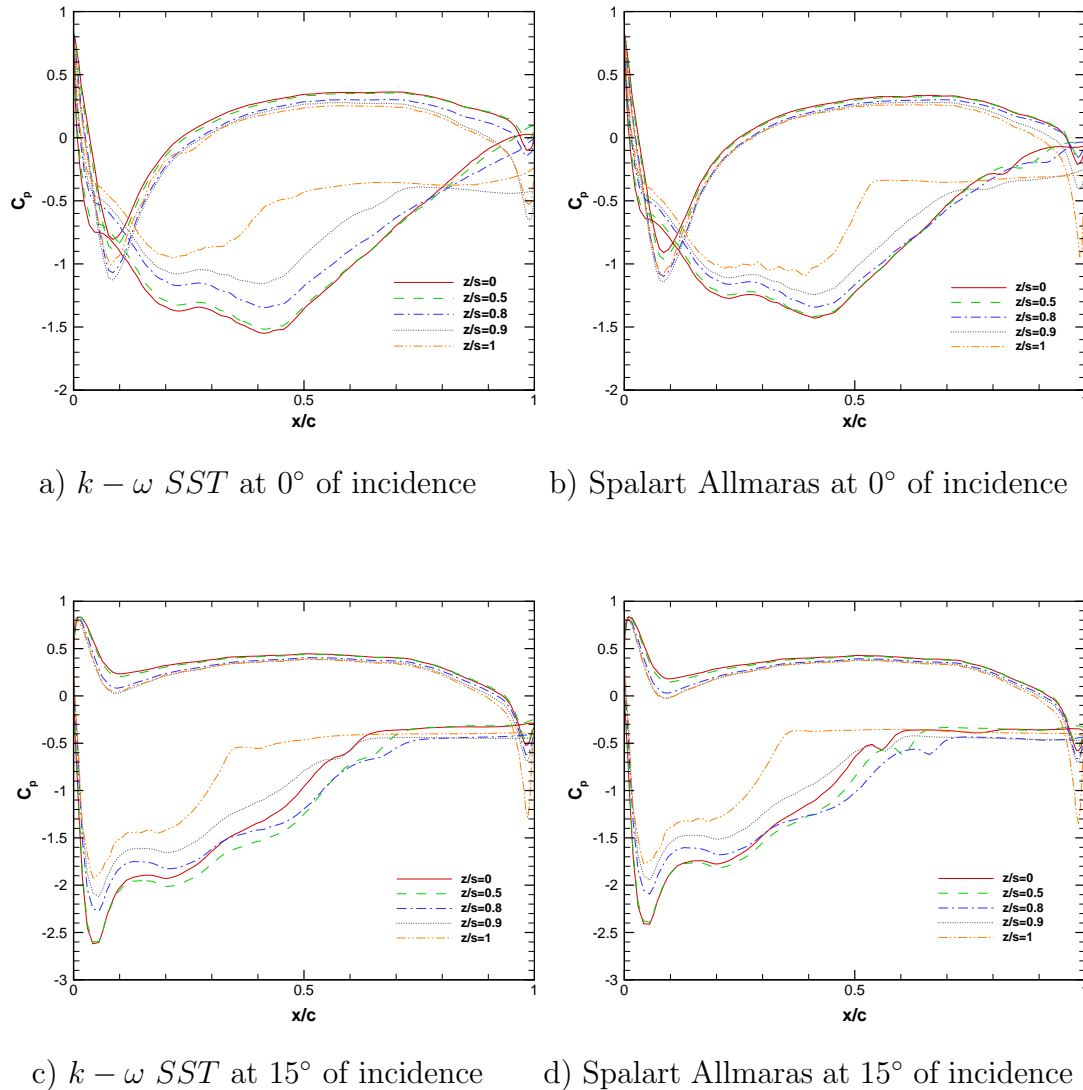
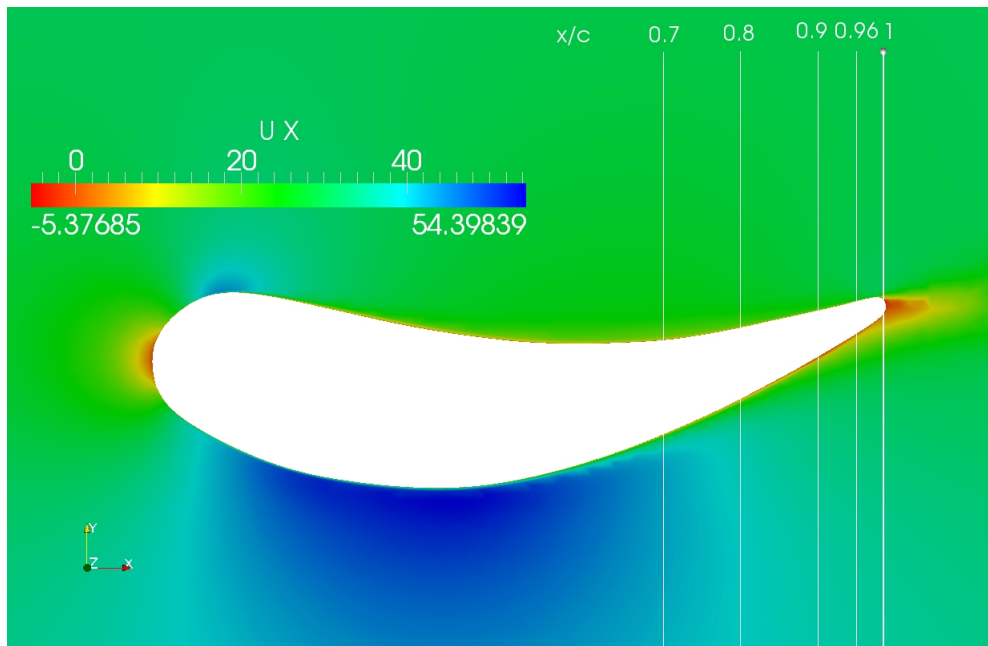


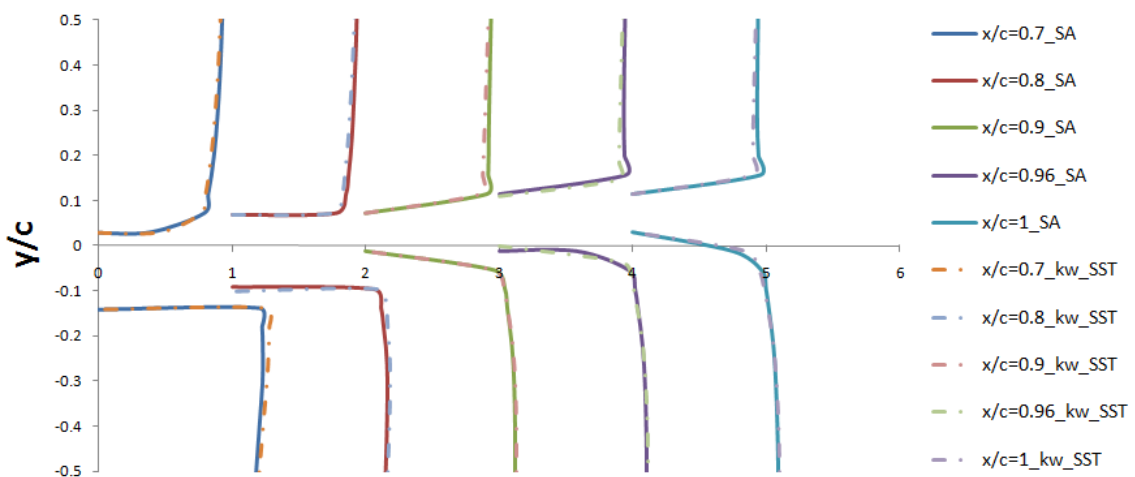
Figure 5.14: Chordwise surface pressure distributions at five cross sections in the spanwise direction

The behavior of the boundary layer on the wing surface can be described by observing the variation of the velocity profiles along the chordwise direction. Figure 5.15 part a) shows the variation of the velocity profiles along the top and bottom wing surfaces for a cross section located in the middle of the wing along five lines as shows figure 5.15 part a). Here, one can observe that the velocity on the suction surface attains a maximum value of 1.3 times the

velocity in the free stream at  $0.7c$ , but it decreases in the streamwise direction. Despite the fact that the velocity contour shows that there exist zones with negative velocities, the profiles show no separation zones on this surface, which suggests that a very small recirculation zone must be located at the tip of the trailing edge. The velocity, on the top surface, attains lower values of velocity, which increase near the trailing edge. Comparing both turbulence models, it is possible to observe that both predicted similar velocity profiles, since for lower angles of attack the adverse pressure gradient is not enough to influence negatively the velocity field inside the boundary layer.



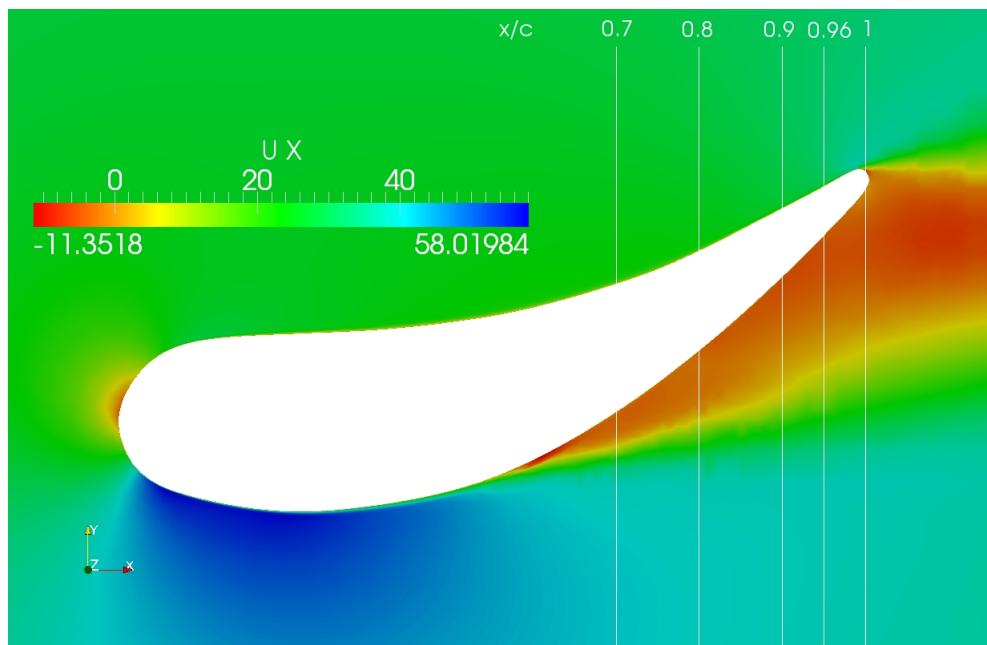
a) Sample lines position



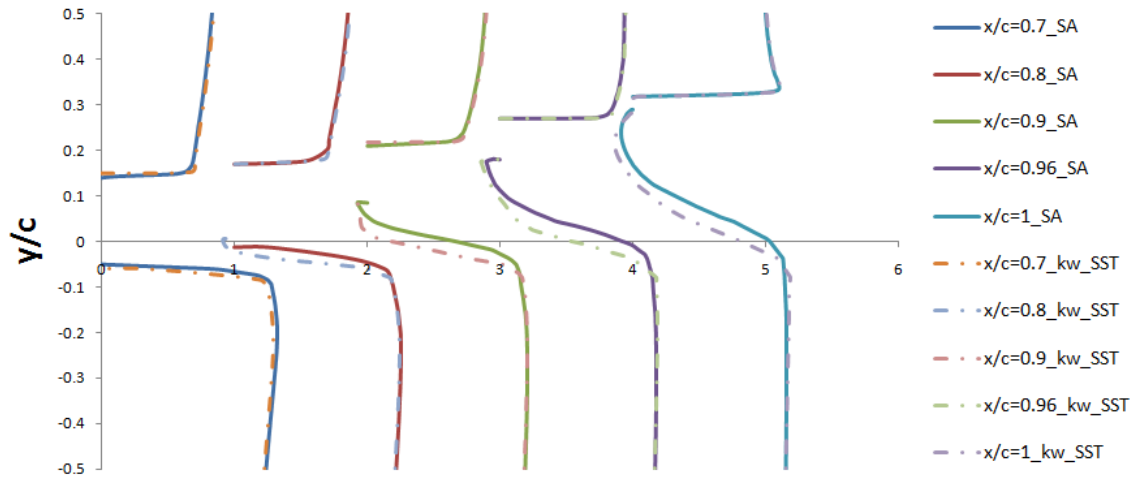
b) Velocity profiles at  $15^\circ$  of incidence

Figure 5.15: Velocity profiles over the wing surface for  $0^\circ$  of incidence

Figure 5.16 part b) shows the variation of the velocity profiles along the top and bottom wing surfaces for a cross section located in the middle of the wing along five lines as shows figure 5.16 part a). Here, we can see that the velocity profiles on the top and bottom of the wing surface are completely different. At the top surface, there is only a little variation in the velocity profiles until  $0.96c$  where the velocity increases due to the airfoil curvature. While at the bottom surface, it is possible to observe that the adverse pressure gradient, produced by the fluid deceleration, influences negatively the velocity field inside the boundary layer, imposing a retarding force in addition to the viscous shears. Its effects can be observed from  $0.8c$  where the boundary limit starts to separate, until  $1c$  where the boundary-layer separation is larger. Comparing both turbulence models, it can be seen that in this particular case, where the adverse pressure gradient is considerable, the velocity profiles predicted by the Spalart Allmaras model and the  $k - \omega/SST$  model presents differences. The Spalart Allmaras model predicted lower separation than the  $k - \omega/SST$  model, which could suggests that the former models is less sensible to the influence of adverse pressure gradients acting on the velocity field near the wall.



a) Sample lines position



b) Velocity profiles at 15° of incidence

Figure 5.16: Velocity profiles over the wing surface for 15° of incidence

### 5.2.5 Flow Visualization

The difficulty involving the experimental visualization and measurement of aerodynamic flows makes CFD simulations a very useful tool to get a deeper insight into the flow physics. In the present study, since only Average Navier-Stokes equations were used to model the turbulence, none of the transient features of vortex structures was observed. However, important features such as vortex origin and its development downstream can help to gain more insight into its nature.

The origin and development of a tip vortex is shown in Fig 5.17. In this figure, a number of streamlines are used to depict the flow around the wing tip. Here, the streamlines are distorted when they arrive at the wing, firstly at the top of the end plate. From that point onwards, the strong pressure difference between the upper and lower wing surfaces twists the streamlines towards the inner plane generating the first vortex. Meanwhile, at the rear part of the wing as well as at the lower part of the end plate, a strong negative pressure field along with the massive pressure difference between the upper and lower wing surfaces generates a central vortex behind the wing and a second vortex at the lower edge of the end plate. The stronger vortex alters the trajectory of the weaker ones, that travels upward. Further downstream, the three vortex merges in one, which continues growing in the streamwise direction.

Other very practical, qualitative analysis of the flow behavior around the wing is that based on iso-contours of the coherence parameter  $Q$ . According to this criterion, the coherence of the vortices can be measured by the second invariant of velocity gradient, defined as.

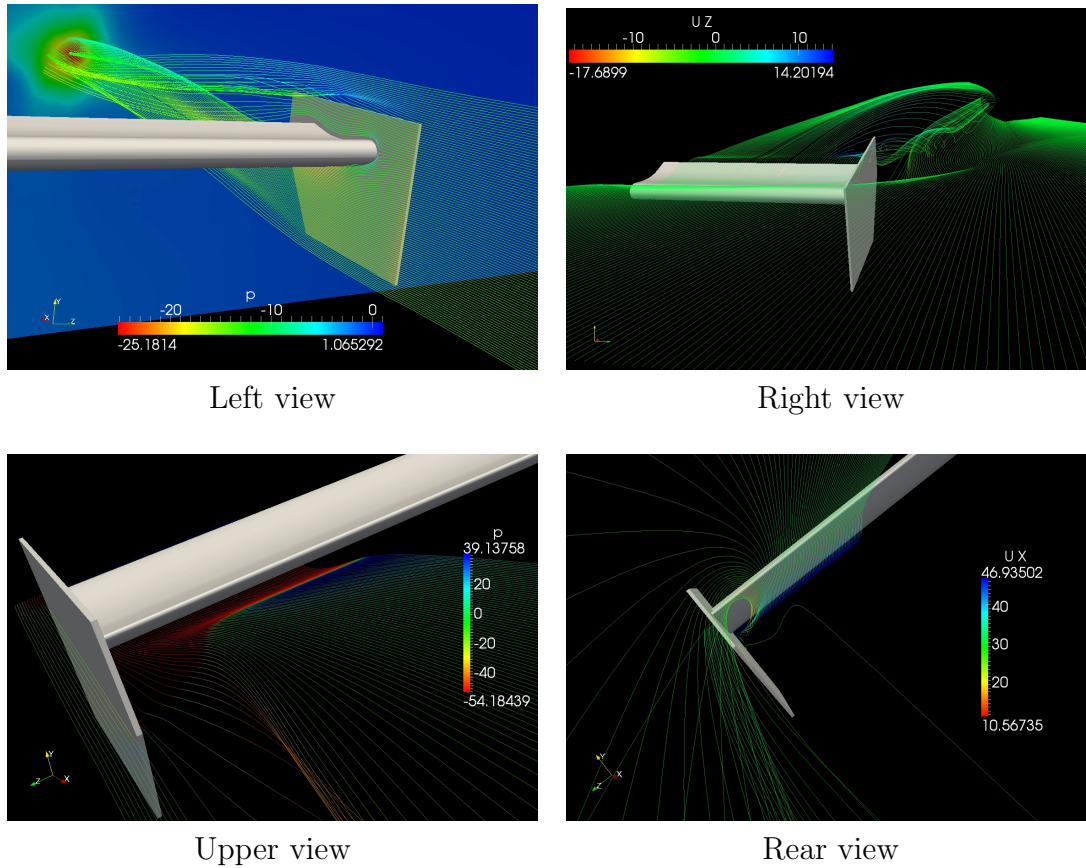


Figure 5.17: Streamlines showing the wing tip vortex development

$$Q = \frac{1}{2} (\bar{S}_{ij} \bar{S}_{ij} - \bar{\Omega}_{ij} \bar{\Omega}_{ij}) , \quad (5.2.1)$$

where

$$\bar{S}_{ij} = \frac{1}{2} \left( \frac{\partial \bar{u}_i}{\partial x_j} + \frac{\partial \bar{u}_j}{\partial x_i} \right) , \quad \bar{\Omega}_{ij} = \frac{1}{2} \left( \frac{\partial \bar{u}_i}{\partial x_j} - \frac{\partial \bar{u}_j}{\partial x_i} \right) , \quad (5.2.2)$$

The coherent structures are those shown when the value of  $Q$  exceeds a certain positive threshold, arbitrarily chosen [29].

Figure 5.18 and figure 5.19 depict the iso-surfaces based on the  $Q$  values for  $0^\circ$   $15^\circ$  of incidence, respectively. In this figure, the origin and development of the aforementioned tip vortices can be observed. Two small coherent structures emerge from the upper and lower edges of the end plate, whereas a massive coherent structure located at the lower rear part of the wing, specifically at the junction of the wing with the end plate, gives rise to the main vortex.

Furthermore, a minor vortex is formed at the interior face of the end plate, which spins contouring the wing leading edge, for both angles of attack. This type of vortex, namely horseshoe vortex, is commonly found in the junction of blunt bodies and walls. It is produced by an upstream boundary layer on a surface that encounters an obstacle attached to that surface. The streamwise

pressure gradients causes the approaching boundary layer to separate and form the horseshoe vortex, whereas the pressure difference between the wing surfaces causes the near-wall flow to move around the obstacle [18].

Small coherent structures are also observed on the lower wing surface and on the interior face of the end plate. It seems that these structures are recirculation zones, related to local boundary layer separations. Since these structures are magnified in the case of the larger angle of incidence, its origin is attributed to the influence of the extensive pressure gradient at the suction zone.

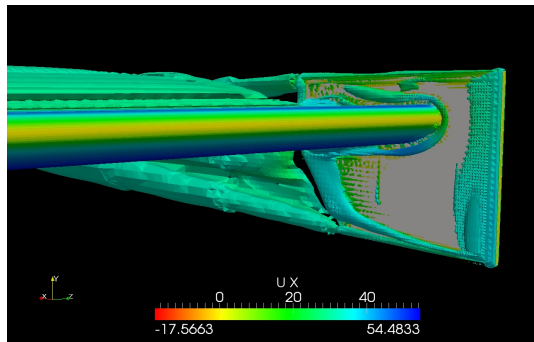
To understand in a better way the interaction among the three vortices originated at the wing tip, figure 5.20 shows contours of time averaged axial velocity in cross planes at different streamwise locations. Here, the size and location of these vortices can be observed clearly as they travel downstream. The central vortex arises from the very low velocity zone in the corner formed by the wing and the end plate, after which it is stretched and split forming two cores. Two additional small vortices arise from the edges of the end plate, which merges with the central ones forming a single core, which becomes more regular and stable as it travels downstream.

An important feature to be considered is that the axial velocity ( $x$  direction) of the vortices is lower than the freestream velocity. According with Galoul and Barber [35], this comes from the fact that the high rate of rotation reduces the pressure at the core, and thus, the air is slowed down in the axial direction.

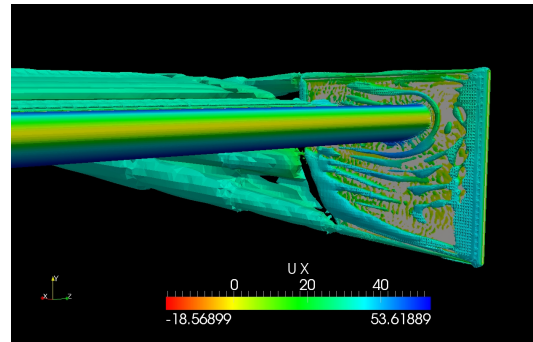
Figure 5.21 shows the contours of mean pressure on some planes at different streamwise locations. Here, the vortex cores are represented by low pressure areas. Immediately after the end plate trailing edge, the core of the vortex originated at the bottom of the end plate, is larger and presents a lower pressure than that originated in the junction between the wing and the end plate. This feature is the result of the influence of the strong pressure difference in the suction zone. However, as the vortices travel downstream, the central one is fed with the strength of the minor vortices until a complete merging in a single vortex takes place.

Figure 5.22 shows contours of time averaged axial vorticity in cross planes at different streamwise locations. Here, one can note the interaction between the top and bottom vortex with the core of the central vortex. These cores are characterized by a high value of vorticity in the positive direction of  $x$ . Moreover, it can be noted in the same figure the presence of an area of negative vorticity on the side of the central vortex. One can consider this area as a counter-rotating secondary vortex, which could be the responsible for the

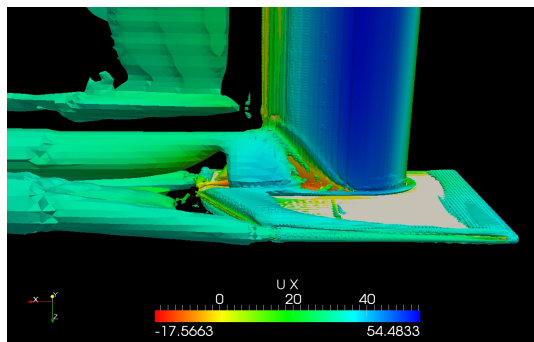
central-vortex core division.



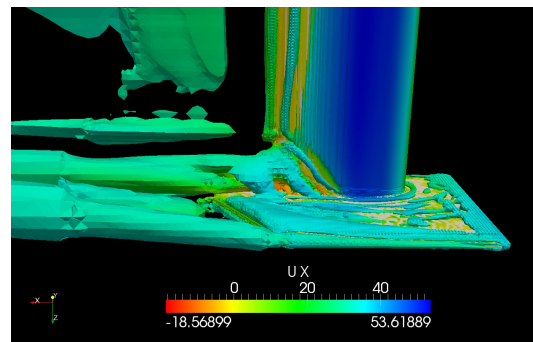
a) Front view  $k - \omega$  SST



b) Front view Spalart Allmaras

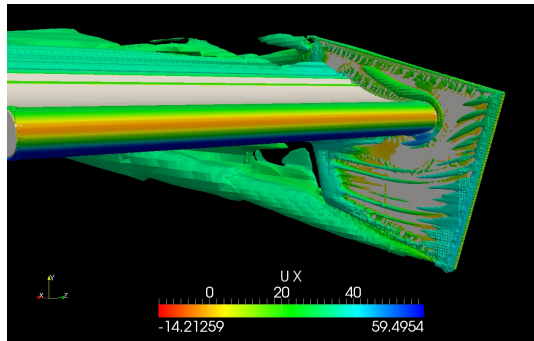
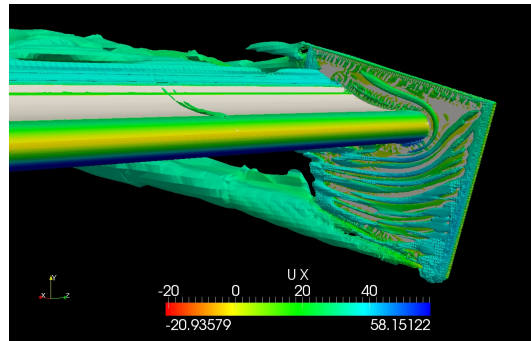


c) Lower surface view  $k - \omega$  SST

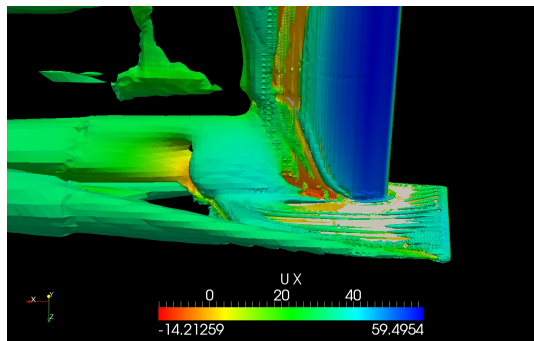
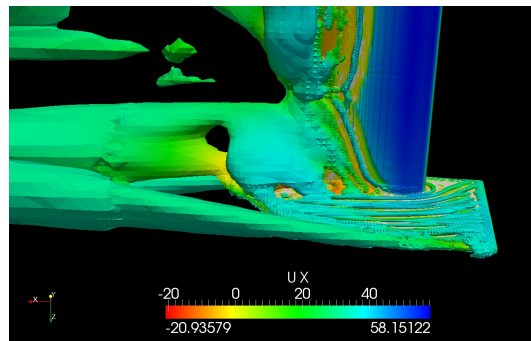


d) Lower surface view Spalart Allmaras

Figure 5.18: Coherent structures around the wing for  $Q = 200$  and  $0^\circ$  of incidence

a) Front view  $k - \omega$  SST

b) Front view Spalart Allmaras

c) Lower surface view  $k - \omega$  SST

d) Lower surface view Spalart Allmaras

Figure 5.19: Coherent structures around the wing for  $Q = 200$  and  $15^\circ$  of incidence

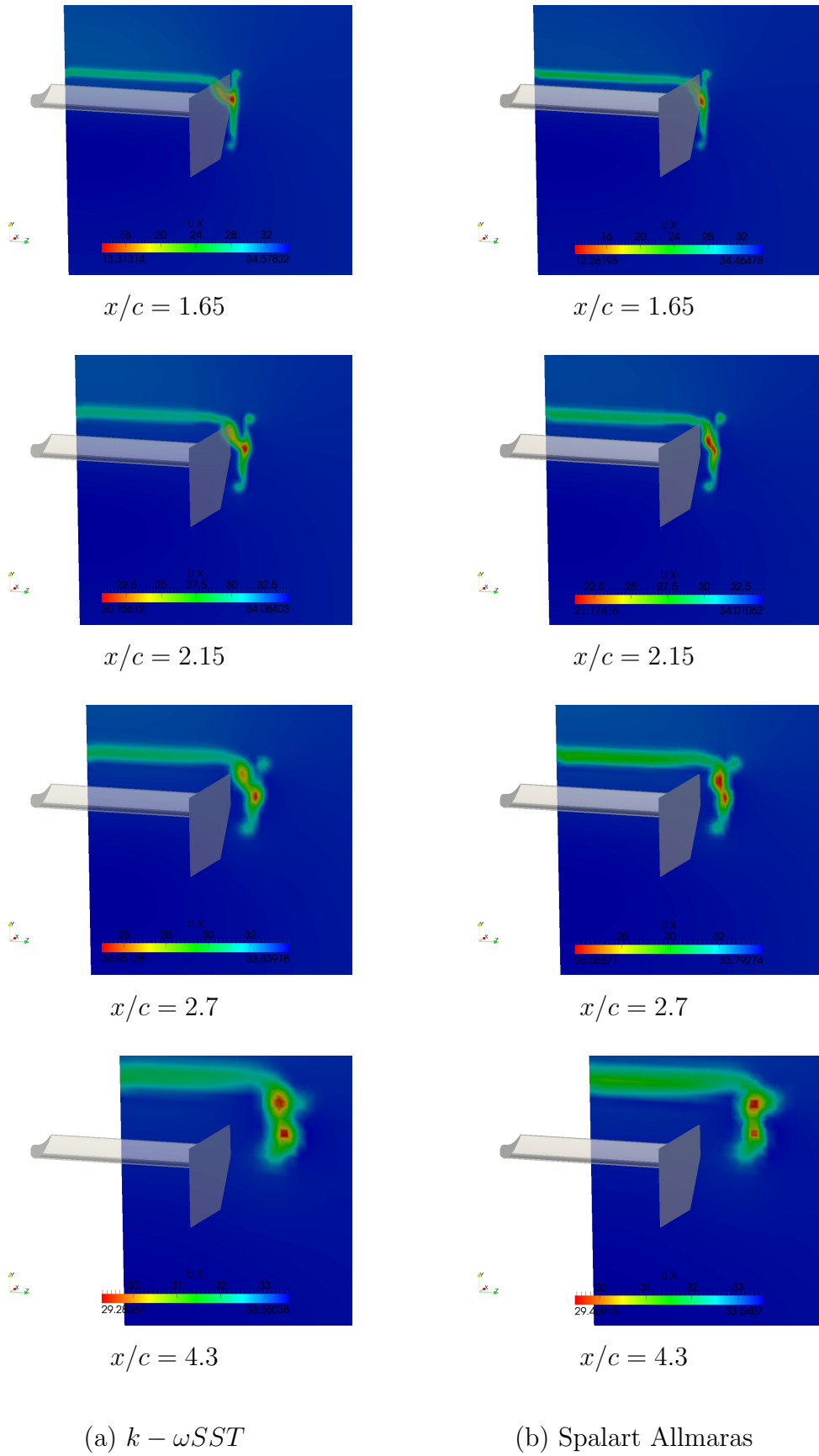
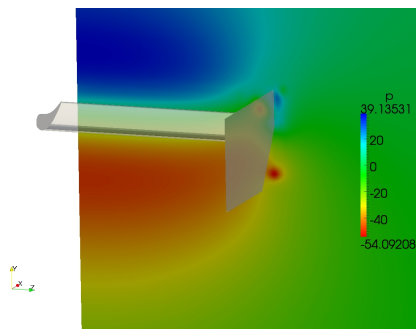
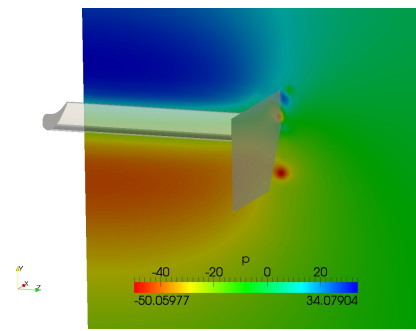


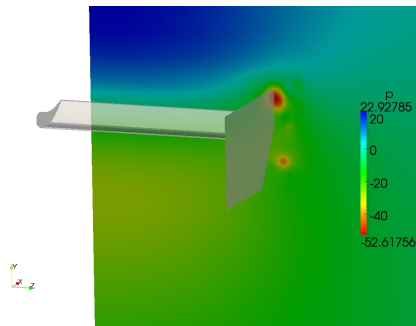
Figure 5.20: Computed velocity contour on cross sections at different stream-wise locations



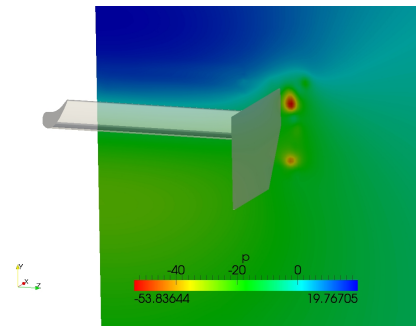
$x/c = 1.65$



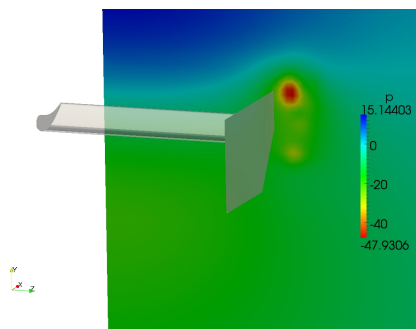
$x/c = 1.65$



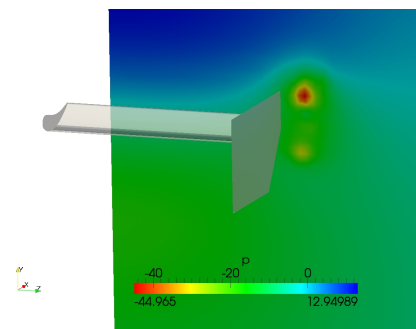
$x/c = 2.15$



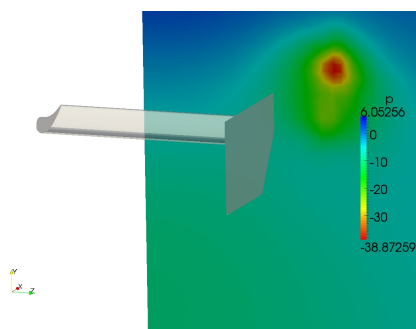
$x/c = 2.15$



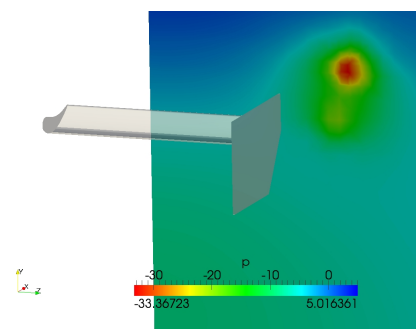
$x/c = 2.7$



$x/c = 2.7$



$x/c = 4.3$



$x/c = 4.3$

(a)  $k - \omega SST$

(b) Spalart Allmaras

Figure 5.21: Computed pressure contour on cross sections at different stream-wise locations



### 5.3

#### Discussion

Regarding the results of the grid refinement study. The use of relatively high aspect ratio cells near the wall with further refinement in the regions of greater curvature, is an interesting strategy to generate an affordable mesh. This was evidenced by the good results obtained with [M10]. In fact, the results obtained using this grid were as good as those obtained using the finest grid [M21] for both turbulence models. In the same manner, when looking for more affordable grids, a coarse grid such as [M15], whose  $y^+$  values are above 30, is a good option.

As a matter of fact, it was observed that there exist considerable numerical diffusion in the regions where the change of the refinement level occurs. Besides, the level of refinement was not enough to represent correctly the gradients involving the vortex region, since the vortex interactions lasted more than five chord lengths downstream. These facts, however, did not affected directly the computation of the flow field around the wing, but correcting them could lead to improve the computation of the downstream flow.

According to the results of lift and drag coefficients, it seems that the airfoil shape used in this wing possess a favorable feature to be used in a race car wing. Its increased camber, aimed at producing an improved lift/drag ratio, may be useful in high speed circuits. However, features such as the excessive thickness just after the leading edge on the upper surface and the excessive curvature of the leading edge do not correspond to the desired characteristics for an application of this type, because they led to a detrimental in the overall airfoil performance. On the other hand, this airfoil shape could not be aimed at producing very high lift due to the reduce lift coefficient and the small frontal area of the wing. In fact, according to the data presented in Selig Michael S. [10], most high cambered airfoils of this type can only be set at maximum  $15^\circ$  of incidence before stalling, which would make imperative the use of a second element, namely flap, to increase the overall lift produced by the airfoil.

Qualitatively, both turbulence models predicted similar pressure distributions in the tip vortex influence zone, for the tested range of angle of attack. However, it should be noted that the  $k - \omega SST$  model predicted greater influence of the tip vortex on the pressure distribution. In this manner, the larger values of lift predicted by this model for higher angles of attack are not only related to the larger velocity computed in the suction surface, but to the positive influence cause by the tip vortex on this region, in the sense that it delays separation. This phenomenon has been described by several authors in the

literature, of which the most related to the subject of this study are those performed to study ground effect on high aspect ratio wings. Despite the fact that in the present study the interaction between the wing and the ground is not significant due to the large distance separating them, it is possible to qualitatively compare the present results with the flow visualization presented by other authors. The studies of Zhang X. et al [21], M. D. Soso and P. A. Wilson [30], and V. Galoul and T.J. Barber [35] showed the presence of two vortices originated from the end plate edges and one originated under the suction surface of the wing, which interact to each other and merge forming a unique core downstream. Among the most important features, described by the aforementioned authors, are the rapid growth of the vortices with downstream distance, the low axial velocity of the central vortex and, more importantly the influence of the central vortex on the pressure field at the suction surface. The last feature can be more clearly observed in two of the above reports [21] ,[30]. There, by means of oil visualization technique, the surface streamlines show the origin of the central vortex just in the line of maximum pressure value on the suction surface, at the junction of the end plate and the suction surface. Equally important is the effect of this vortex on the nearest flow region, where the induced flow delays the boundary layer separation. Zhang X., et al [21], describes this phenomenon as being caused by the effective reduction in the incidence due to the tip vortex, or in other words, the upwash produced by the tip vortex.

This description agrees with the findings exposed in the present study and helps to confirm the suitability of both the grid and the turbulence models employed in this study in order to generate useful data for the analysis and development of aerodynamic devices. This is not to say, the results of the three-dimensional simulation correspond to real values, as to assert this, it would be necessary an extensive validation comparing aerodynamic forces and the structure of the flow field around the wing with experimental data. Notwithstanding the lack of experimental data, the simulations accuracy (despite all its intrinsic uncertainties, like grid, turbulence models, etc.) seemed to be enough to capture the essential physics. In the near future, with the availability of experimental data it will be possible to know how reliable this methodology is, and whether it is ready to be employed for the analysis and development of aerodynamic devices.